Directional Thermal Diffusion Realizing Inorganic Sb2Te3/Te Hybrid Thin Films with High Thermoelectric Performance and Flexibility

Meng Wei, Xiao-lei Shi, Zhuang-Hao Zheng, Fu Li, Wei-Di Liu, Li-Ping Xiang, Yang-Su Xie, Yue-Xing Chen, J.-Y. Duan, Hong-Li Ma, et al.

Directional Thermal Diffusion Realizing Inorganic Sb_2Te_3/Te Hybrid Thin Films with High Thermoelectric Performance and Flexibility

Meng Wei, Xiao-Lei Shi, Zhuang-Hao Zheng, Fu Li, Wei-Di Liu, Li-Ping Xiang, Yang-Su Xie, Yue-Xing Chen, Jing-Yi Duan, Hong-Li Ma, Guang-Xing Liang, Xiang-Hua Zhang, Ping Fan, and Zhi-Gang Chen**

Inorganic films possess much higher thermoelectric performance than their organic counterparts, but their poor flexibilities limit their practical applications. Here, Sb_2Te_3/Te_x hybrid thin films with high thermoelectric performance and flexibility, fabricated via a novel directional thermal diffusion reaction growth method are reported. The directional thermal diffusion enables rationally tuning the Te content in Sb_2Te_3, which optimizes the carrier density and leads to a significantly enhanced power factor of >20 μW cm^{-1} K^{-2}, confirmed by both first-principles calculations and experiments; while dense boundaries between Te and Sb_2Te_3 nanophases, contribute to the low thermal conductivity of ≈0.86 W m^{-1} K^{-1}, both induce a high *ZT* of ≈1 in $(Sb_2Te_3)(Te)_{1.5}$ at 453 K, ranking as the top value among the reported flexible films. Besides, thin films also exhibit extraordinary flexibility. A rationally designed flexible device composed of $(Sb_2Te_3)(Te)_{1.5}$ thin films as *p*-type legs and Bi_2Te_3 thin films as *n*-type legs shows a high power density of >280 μW cm^{-2} at a temperature difference of 20 K, indicating a great potential for sustainably charging low-power electronics.

1. Introduction

With the rapid development of micro-electromechanical systems and the continuous emergence of smart wearable devices, searching for sustainable, self-power, and maintenance-free power supply technologies is highly needed.[1] Compared to traditional batteries, which require regular replacement, charging, and maintenance, flexible or miniatured thermoelectric devices can collect heat from the surrounding environment to realize long-term power supply,[2] and show high flexibility and adaptability to various working conditions in the fields of Internet of Things, sensors, and mobile/wearable electronics.[3–6] In these flexible or miniatured thermoelectric devices, inorganic thermoelectric films possess

M. Wei, Z.-H. Zheng, F. Li, Y.-X. Chen, G.-X. Liang, P. Fan
Shenzhen Key Laboratory of Advanced Thin Films and Applications
Key Laboratory of Optoelectronic Devices and Systems of Ministry of Education and Guangdong Province
College of Physics and Optoelectronic Engineering
Shenzhen University
Shenzhen 518060, P. R. China
E-mail: zhengzh@szu.edu.cn

X.-L. Shi, Z.-G. Chen
School of Chemistry and Physics
Queensland University of Technology
Brisbane, Queensland 4001, Australia
E-mail: zhigang.chen@qut.edu.au

The ORCID identification number(s) for the author(s) of this article can be found under https://doi.org/10.1002/adfm.202207903.

DOI: 10.1002/adfm.202207903

W.-D. Liu
Australian Institute for Bioengineering and Nanotechnology
The University of Queensland
Brisbane, Queensland 4072, Australia

L.-P. Xiang, Y.-S. Xie
College of Chemistry and Environmental Engineering
Shenzhen University
Shenzhen, Guangdong 518055, P. R. China

J.-Y. Duan
Centre for Quantum Physics
Key Laboratory of Advanced Optoelectronic Quantum Architecture and Measurement (MOE)
College of Physics
Beijing Institute of Technology
Beijing 100081, P. R. China

H.-L. Ma, X.-H. Zhang
Univ Rennes
CNRS
ISCR (Institut des Sciences Chimiques de Rennes) UMR6226
Rennes F-35000, France

much higher thermoelectric performance than their organic counterparts.[3,7] Their performance is generally evaluated by the dimensionless figure-of-merit ZT,[8] which is defined by $ZT = S^2\sigma T/\kappa$, where S, σ, T, and κ are Seebeck coefficient, electrical conductivity, absolute temperature, and thermal conductivity, respectively. $S^2\sigma$ is described as a thermoelectric power factor, and κ is usually composed of electronic and lattice thermal conductivities (κ_e and κ_l).[1] To achieve high ZT values, it is necessary to increase their S and σ, and correspondingly reduce their κ. However, these three parameters are coupled with each other by the carrier density (n_p for p-type materials with holes as major carriers, and n_e for n-type materials with electrons as major carriers).

Among inorganic thermoelectric films,[3,9] p-type Sb_2Te_3 is a narrow-bandgap semiconductor (0.3 eV),[10] and has good thermoelectric properties at near room temperature.[11,12] Various techniques, such as thermal evaporation,[10] sputtering,[13,14] electrochemical deposition,[15] molecular beam epitaxy (MBE),[16] pulsed laser deposition (PLD),[17] chemical vapor deposition (CVD),[18] are widely used to fabricate Sb_2Te_3-based thin films. Heat treatment,[19] orientation control,[9] and doping are also used to further improve their σ.[20] Among them, heat treatment and orientation control can reduce carrier scattering and improve carrier mobility μ, and doping with appropriate elements can tune n_p. As well, the improvement of the S is mainly achieved by using the energy filtering effect.[21] Introducing nanoinclusions into the Sb_2Te_3 matrix can rationally filter carriers to increase the energy dependence of the carrier relaxation time and in turn improve the S.[22,23] Moreover, superlattice,[24] organic-inorganic hybridization,[25] and solid solution[26] are effective methods to reduce κ_l. Among them, superlattices can effectively scatter phonons due to their special structure, which significantly reduces the κ_l.[24] By using organic-inorganic hybridization, the combination of Sb_2Te_3 with good electrical properties and organic compounds with low κ can realize the complementary advantages of different materials.[27] The solid solution of Bi_2Te_3 and Sb_2Te_3 can introduce a large number of point defects in Sb_2Te_3, which strongly scatters phonons. Benefiting from the synergetic effect of the above advanced strategies, high thermoelectric properties with ZTs of >1 have been achieved in Sb_2Te_3-based solid films.[1,13,14] However, there are still many challenges to employing Sb_2Te_3-based thermoelectric thin films in practical applications because of their poor flexibility, unsatisfied thermoelectric devices, and low device energy conversion efficiency of devices.[3,28–30]

To achieve both high thermoelectric performance and flexibility, here, we fabricate inorganic $(Sb_2Te_3)(Te)_x$ hybrid thin films by using a novel directional thermal diffusion reaction growth method (Figure S1 in the Supporting Information). Compared with previously reported fabrication routes,[31] the direction of heating is strictly from bottom to top instead of overall heating, so the uniformity and quality of the as-fabricated film are both better. We perform the first-principles density functional theory (DFT) calculations to investigate the electronic band structures (**Figure 1**a,b) and the density of states (DOS) (Figure 1c) of Sb_2Te_3 and Te. As can be seen, Sb_2Te_3 and Te have similar bandgap values while the DOS of Te is much smaller than that of Sb_2Te_3, suggesting that introducing a certain amount of Te into Sb_2Te_3 can appropriately reduce the overall DOS and in turn the n_p of the mixed system and improve the S. At the same time because practical Sb_2Te_3 and Te are both p-type conductive,[32] and there is no potential barrier between the two materials due to the similar bandgap, the carriers may not be obviously scattered at the interfaces to improve the μ, leading to improved σ. Besides, according to the defect formation equation, described as $Sb_2Te_3 \leftrightarrow 2Sb'_{Te} + 5/2Te_2(g) + 2\,h$,[33] and the fact that Sb'_{Te} anti-site defects are commonly found in undoped Sb_2Te_3-based thin films, introducing extra Te in the hybrid can suppress the releasing of holes, leading to suppressed n_p. Based on these strategies, we rationally tune the content of Te in Sb_2Te_3 to reduce the n_p, leads to significantly enhanced $S^2\sigma$ of $(Sb_2Te_3)(Te)_{1.5}$ hybrid thin film. At the same time, introducing Te in Sb_2Te_3 results in dense phase boundaries between Te and Sb_2Te_3 nanophases, contributing to a low κ_l. As a result, we achieve a high ZT of ≈1 in $(Sb_2Te_3)(Te)_{1.5}$ at 453 K, which ranks as the top value among the reported flexible thermoelectric films,[34–39] as shown in Figure 1d. Meanwhile, an ultralow normalized resistance R/R_0 (R_0 is the initial resistance and R is the resistance after bending) of ≈1.07 is achieved after 2000 bending cycles with a minimum bending radius r of only 6.5 mm, indicating significantly competitive flexibility,[34,40–43] as shown in Figure 1e and Table S1 (Supporting information). Furthermore, a rationally designed flexible thermoelectric device, assembled by $(Sb_2Te_3)(Te)_{1.5}$ thin films as p-type legs and Bi_2Te_3 thin films as n-type legs (Figure S2, Supporting Information), shows a competitively high power density ω_{out} of ~0.3 mW cm^{-2} by a temperature difference ΔT of 20 K,[44–49] as shown in Figure 1f, indicating great potential for applying to practical applications.

2. Results and Discussions

To explore the best Te concentration for optimizing the thermoelectric performance of Sb_2Te_3-based flexible thin films, we design the compositions of the Sb_2Te_3/Te hybrid thin films, described as $(Sb_2Te_3)(Te)_x$, where x = 0, 0.5, 1, 1.5, and 2. The detailed fabrication methods for $(Sb_2Te_3)(Te)_x$ thin films and their related devices can be referred to Figures S1 and S2 in the Supporting Information. To study the phase information of the as-fabricated thin films, X-ray diffraction (XRD) was investigated. **Figure 2**a shows XRD patterns of $(Sb_2Te_3)(Te)_x$ thin films. All peaks can be indexed to Sb_2Te_3 (PDF #15-0874) and Te (PDF #36-1452), and preferential growth along the (015) plane can be observed in Sb_2Te_3 thin films, indicating obvious anisotropy. As well, with increasing the x, the (101) and (031) peaks of Te become more intensive, indicating the increase of Te content in Sb_2Te_3 thin films. It should be noted that even for the Sb_2Te_3 thin film without extra Te (x = 0), Te is still found in Sb_2Te_3 thin films. The energy dispersive spectroscopy (EDS) results indicate that the practical atomic ratio of Sb:Te is 2:3.14 (Table S2, Supporting Information), indicating extra Te in Sb_2Te_3 thin film. Figure 2b shows Raman spectra of $(Sb_2Te_3)(Te)_x$ thin films (x = 0, 0.5, 1, 1.5, and 2), and Figure 2c illustrates the crystal structure of Sb_2Te_3. The three Raman vibration modes, located at 68.5, 112.5, and 165.5 cm^{-1}, are attributed to the A^1_{1g}, E^2_g, and A^2_{1g} of Sb_2Te_3 (Figure 2d). With increasing the x, the Raman peak of Te gradually appears with the three

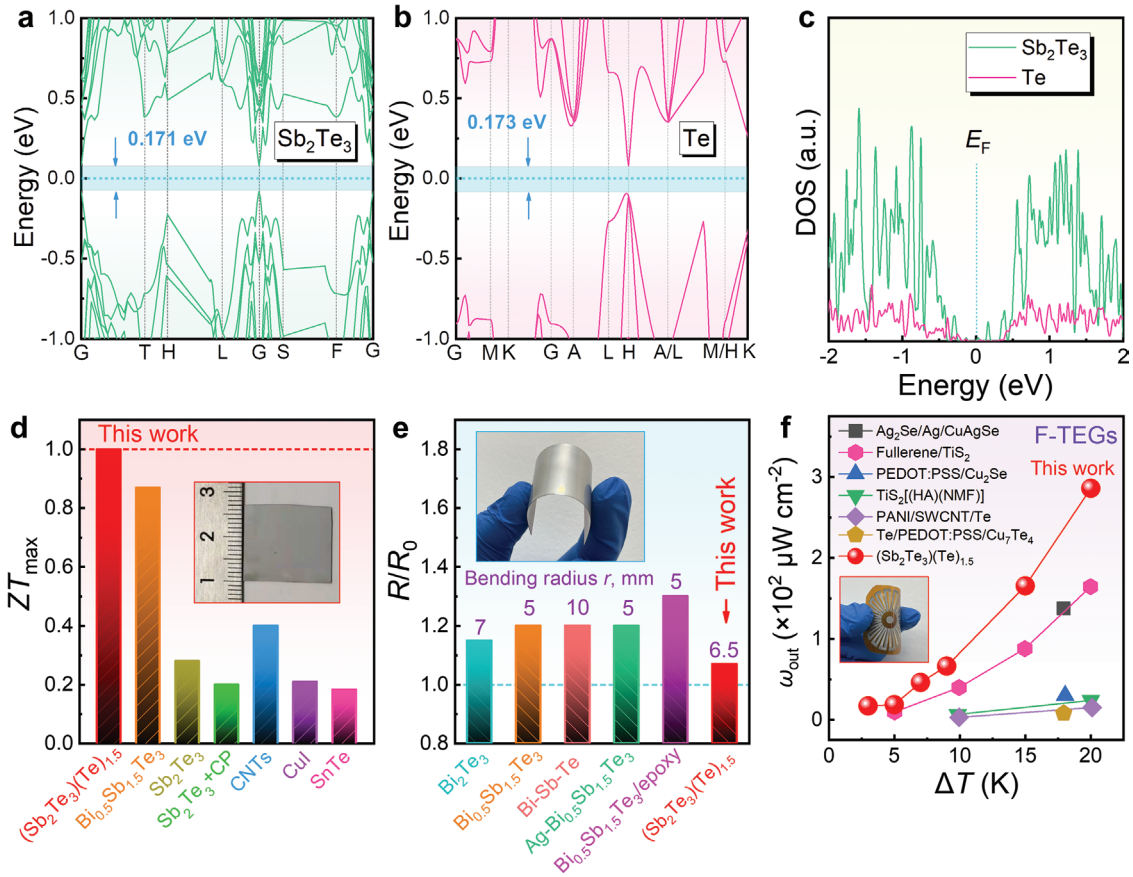

Figure 1. Calculated band structures of a) Sb_2Te_3 and b) Te, and c) corresponding density of states (DOS) of Sb_2Te_3 and Te. Here E_F is the Fermi level. d) Comparison of maximum dimensionless figure-of-merit ZT (ZT_{max}) for *p*-type flexible thermoelectric films between $(Sb_2Te_3)(Te)_{1.5}$ hybrid thin film (this work) and reported literature.[34–39] The phono of as-fabricated thin film is shown as an inset. e) Comparison of normalized resistance R/R_0 (R_0 is the initial resistance and R is the resistance after bending) between this work and reported literature.[34,40–43] The minimum bending radius r values are provided. The phono of bending the as-fabricated thin film is shown as an inset. f) Comparison of output power density ω_{out} for flexible thermoelectric generators (F-TEGs) between $(Sb_2Te_3)(Te)_{1.5}$ thin-film-based device (this work) and reported literature as a function of temperature difference ΔT (here $\Delta T \leq 20$ K).[44–49] The phono of bending the as-fabricated device is shown as an inset.

active Raman phonon modes, E^1, A^1, and E^2 (Figure 2e). The most intense Raman peak of Te located at ~121.5 cm^{-1} is related to the A^1 mode, corresponding to the chain expansion mode in which each atom moves in the basal plane. Meanwhile, two degenerate E modes separate into predominately bond-bending and bond stretching types. The E^1 mode at ~86.5 cm^{-1} is caused by *a*-axis rotation, and the E^2 mode at 140.9 cm^{-1} is appointed to asymmetric stretching mainly along the *c*-axis.[34] These results confirm the co-existence of Sb_2Te_3 and Te in the as-fabricated films.

To study the valence states of Sb and Te in the as-fabricated hybrid films, we perform X-ray photoelectron spectra (XPS). Taking $x = 1.5$ for an example, Figure 2f–h show full-spectrum, high-resolution spectrum of Sb 3d, and high-resolution spectrum of Te 3d of $(Sb_2Te_3)(Te)_{1.5}$. The high-resolution spectra of the Sb 3d and Te 3d are obtained using C1s as the reference at 284.6 eV. As shown in Figure 2f, the binding energies corresponding to the energy levels of Sb and Te are clearly detected, and no impurity (including oxygen) peak can be observed in the spectra. The binding energies at 529.81 and 538.78 eV correspond to the Sb $3d_{5/2}$ and Sb $3d_{3/2}$, which are the characteristic peaks of the Sb^{3+} valence state (Figure 2g). The 3d core-level of Te with two peaks at 583.12 and 573.15 eV are shown in Figure 2h, which are related to the binding energy of Te $3d_{3/2}$ and Te $3d_{5/2}$ in Sb_2Te_3. The XPS spectra of Sb and Te are divided into unbound (Sb^0)/bound (Sb^{3+}) and unbound (Te^0)/bound (Te^{2-}),[50] respectively. The bound states of Sb ions (Sb^{3+}) and Te ions (Te^{2-}) were obtained when Te atoms were fully sublimated and diffused into the Sb, and reacted with Sb during the directional thermal diffusion reaction growth process.[31] Unbound Te^0, located at 573.3 eV and 583.9 eV, is also clearly observable on the XPS spectra, indicating the formation of Te in the hybrid films.

To study the morphological and compositional characteristics of the as-fabricated hybrid films, scanning electron microscopy (SEM), transmission electron microscopy (TEM), and spherical aberration-corrected scanning (Cs-STEM) were investigated. **Figure 3**a–e show SEM images of side- and top-views of $(Sb_2Te_3)(Te)_x$ thin films for $x = 0$, 0.5, 1, 1.5, and 2. The side-views are based on the cross-section images. All films show typical dense polycrystalline features, and the corresponding thicknesses of the thin films are 690, 630, 650, 680,

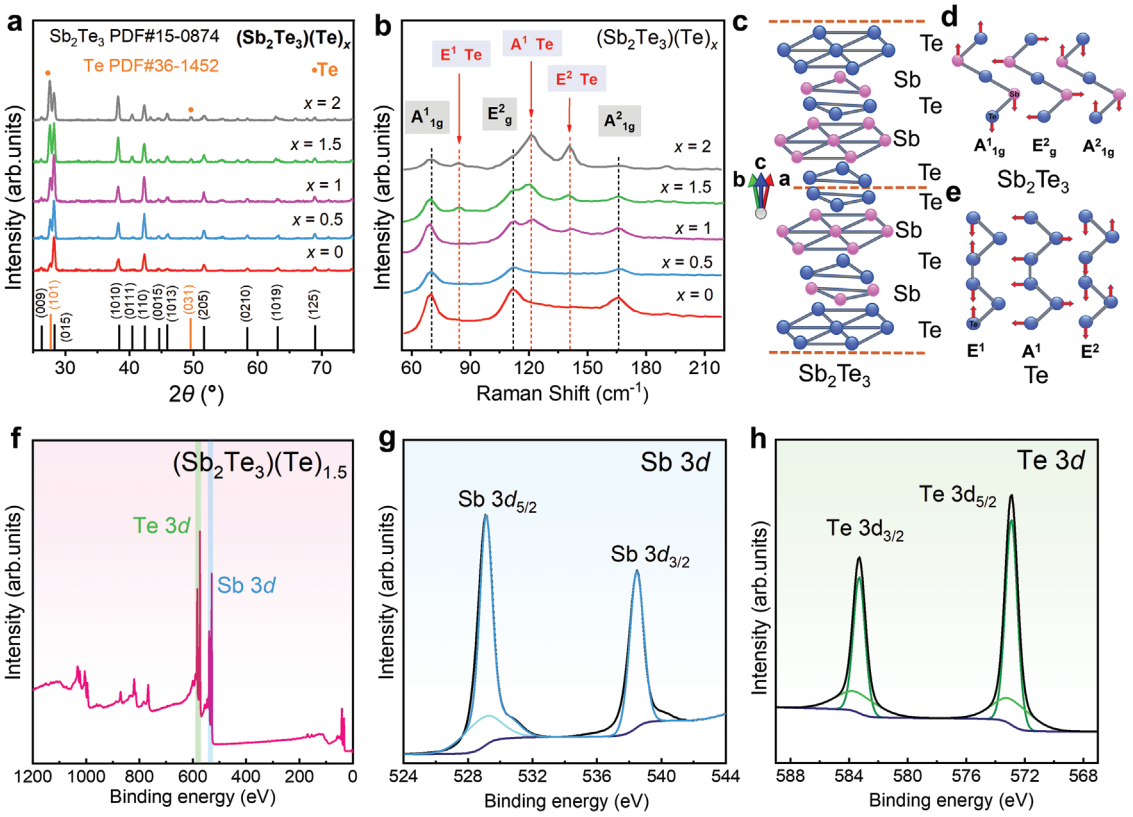

Figure 2. a) X-ray diffraction (XRD) patterns and b) Raman spectra of $(Sb_2Te_3)(Te)_x$ thin films ($x = 0$, 0.5, 1, 1.5, and 2). c) Crystal structure of Sb_2Te_3 and three main Raman-active modes in d) Sb_2Te_3 and e) Te. X-ray photoelectron spectra (XPS) of f) full spectrum, g) Sb 3d, and h) Te 3d of $(Sb_2Te_3)(Te)_{1.5}$.

and 700 nm. The cross-section images clearly indicate that the Te content directly affects the crystal growth, which can be confirmed by the peak intensity change of (015) that belongs to Sb_2Te_3, as shown in Figure 2a. Besides, with the increasing Te content (x value), some crystalline islands appear, especially on the surface of the films. We magnify these crystalline islands as shown in Figure 3f, and two EDS spots are taken from A- and B-sites, from which A-site is taken from the surface of the hybrid film, and B-site is taken from one crystalline island. The EDS spot results indicate that these crystalline islands are typical Te crystals. The EDS maps for the surface of the hybrid film with Te crystalline islands are shown in Figure S3 (Supporting Information) for reference. Figure 3g shows a low-magnification TEM image of the side-view of $(Sb_2Te_3)(Te)_{1.5}$ thin film. The film is covered with a Pt layer for better characterization. Figure 3h is the EDS map taken from Figure 3g for Sb, Te, and Pt. As can be seen, Sb elements are uniformly distributed inside the thin film, while Te elements are not as uniform as Sb elements. Besides, excess Te precipitates on the surface of the Sb_2Te_3 thin film, which are the Te crystalline islands as observed in SEM images. The non-uniform distribution of Te elements in the thin film indicates the potential existence of Te micro/nanophases inside the film. Figure 3i shows a low-magnification TEM image of a sliced $(Sb_2Te_3)(Te)_{1.5}$ thin film, and Figure 3j shows a high-resolution TEM (HRTEM) image taken from Figure 3i to see the nanophases of Sb_2Te_3 (labeled with purple color) and Te (labeled with green color). These results indicate that Te possesses at least two forms of existence in the hybrid films, namely microsized Te crystalline islands and nanosized Te inclusions. The intensive grain and phase boundaries are predicted to effectively scatter the phonons and in turn suppress the κ_l. In terms of the crystalline feature of the main Sb_2Te_3 phase, Figure 3k,l show Cs-STEM high angle annular dark-field (HAADF) images of Sb_2Te_3 phase viewed along the b-axis and in-plane direction. The crystal structure of Sb_2Te_3 viewed along the b-axis and in-plane direction are provided as insets for comparison. These results indicate the high quality of as-growth Sb_2Te_3 crystals. The EDS maps of the thin film based on Cs-STEM are provided in Figure S4 (Supporting Information) for reference.

We carefully evaluate the thermoelectric properties of the as-fabricated hybrid thin films, including σ, S, $S^2\sigma$, n_p, μ, and κ. **Figure 4**a shows temperature-dependent σ of $(Sb_2Te_3)(Te)_x$ hybrid thin films. With increasing the temperature from room temperature to 453 K, σ of all films is decreased, which is the typical semiconducting feature of Sb_2Te_3. As well, with increasing x from 0 to 1, σ is increased, indicating potentially increased n_p or μ; while with increasing x from 1 to 2, σ is decreased, indicating excess Te may damage the electrical transport. Figure 4b shows temperature-dependent S. Compared with Figure 4a, S shows the opposite trends of σ, double-confirming the semiconducting feature of Sb_2Te_3. Interestingly, with increasing x from 0 to 1.5, S is also increased, resulting in high $S^2\sigma$ of >20 μW cm^{-1} K^{-2} within the entire temperature range when $x = 1$, as shown in Figure 4c. Figure 4d compares n_p and μ of the thin films as a function of x. As can be seen, with

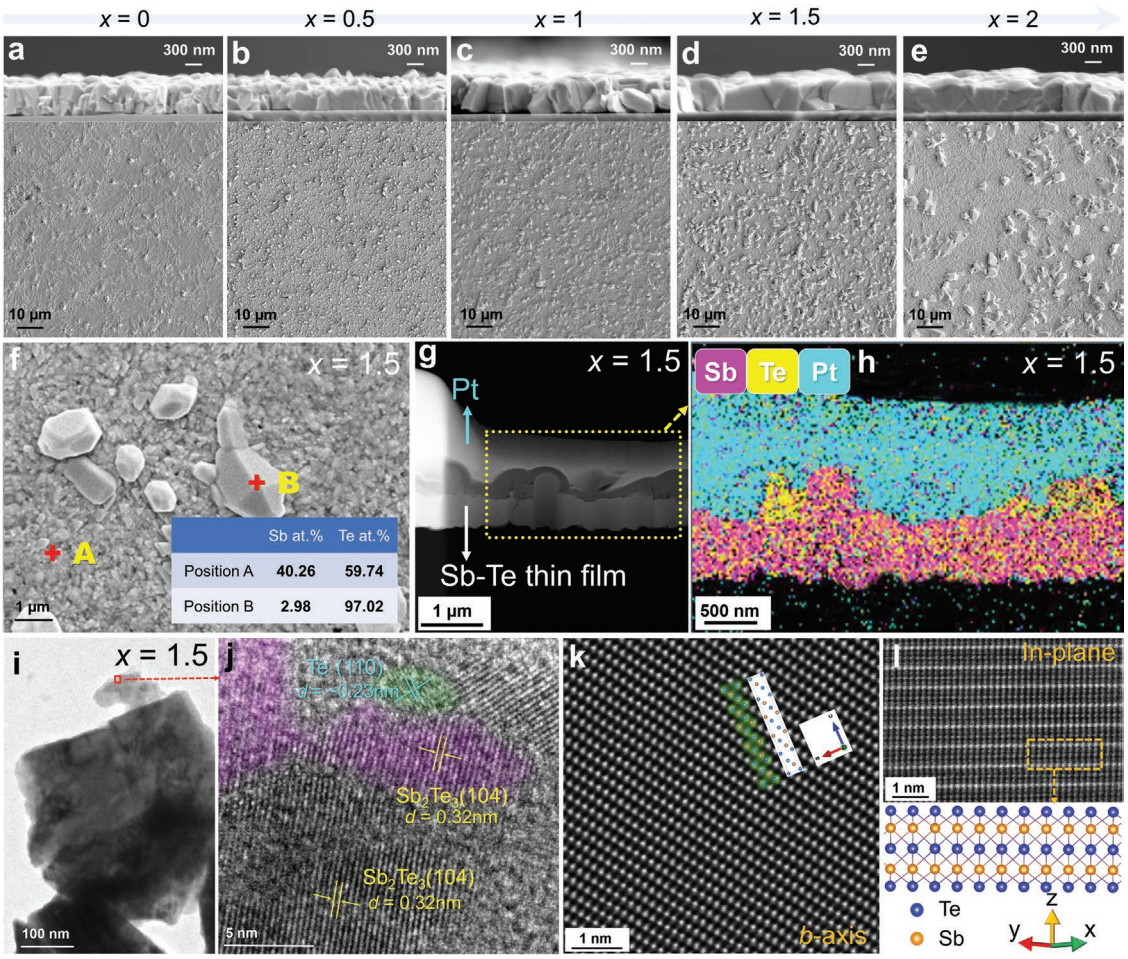

Figure 3. Scanning electron microscopy (SEM) images of side- and top-views of $(Sb_2Te_3)(Te)_x$ thin films for a) $x = 0$, b) $x = 0.5$, c) $x = 1$, d) $x = 1.5$, and e) $x = 2$. f) Magnified SEM image of top-view of $(Sb_2Te_3)(Te)_{1.5}$ thin films. Two energy dispersive spectroscopy (EDS) spots are taken from A- and B-sites. The EDS spot results are shown as an inset. g) Transmission electron microscopy (TEM) image of side-view of $(Sb_2Te_3)(Te)_{1.5}$ thin film. The film is covered with a Pt layer. h) EDS map taken from g for Sb, Te, and Pt. i) TEM image of a sliced $(Sb_2Te_3)(Te)_{1.5}$ thin film. j) High-resolution TEM (HRTEM) image taken from i) to see the nanophases of Sb_2Te_3 (labeled with purple color) and Te (labeled with green color). Spherical aberration-corrected scanning (Cs-STEM) high angle annular dark-field (HAADF) images of Sb_2Te_3 phase viewed along the k) *b*-axis and l) in-plane direction. The crystal structure of Sb_2Te_3 viewed along the in-plane direction is provided in l for comparison.

increasing x from 0 to 1, n_p is decreased and μ is increased. As discussed before, our first-principles DFT calculations indicate that Sb_2Te_3 and Te have similar bandgap values, but the DOS of Te is much smaller than that of Sb_2Te_3, therefore introducing a certain amount of Te into Sb_2Te_3 can appropriately reduce the overall DOS and in turn, reduce the n_p of the mixed system and improve the S. At the same time, because practical Sb_2Te_3 and Te are both p-type conductive,[32] and there is no potential barrier between the two materials due to the similar bandgap, the carriers cannot be obviously filtered or blocked, therefore the increased μ and σ are reasonable due to the less carrier-carrier scattering by the reduced n_p. Besides, according to $Sb_2Te_3 \leftrightarrow 2Sb'_{Te} + 5/2Te_2(g) + 2h^{\cdot}$,[33] introducing extra Te in the hybrid can suppress the releasing of holes, leading to suppressed n_p. However, it should be noted that excessive Te may also reduce the σ. With increasing x from 1 to 2, n_p is increased and μ is decreased. This is because when there is too much Te, a large amount of Sb_2Te_3/Te physical interfaces (phase boundaries between polycrystalline Sb_2Te_3 and both Te crystalline islands and nanosized Te inclusions) significantly scatter carriers again. Considering that there is no obvious energy filtering effect between the Te and Sb_2Te_3 phases, most carriers can only be scattered but not filtered or blocked, resulting in lower μ and in turn higher n_p. Figure 4e shows the calculated effective mass m^* and deformation potential E_{def} as a function of x by a single parabolic band (SPB) model. It should be noted that the SPB model is suitable for evaluating the electrical transport behavior of Sb_2Te_3 when the dominated scattering mechanism is acoustic phonon scattering.[51–56] With increasing the x, m^* has the same trend of n_p, confirming that there is no obvious energy filtering effect at the interfaces of Te and Sb_2Te_3 and m^* directly reflects the variation of n_p. However, with increasing the x, E_{def} is decreased. This is because the E_{def} is related to the structures of the hybrid films, especially for the densities and the velocities of the hybrids. Because the velocity of Te is much smaller than that of Sb_2Te_3 (refer

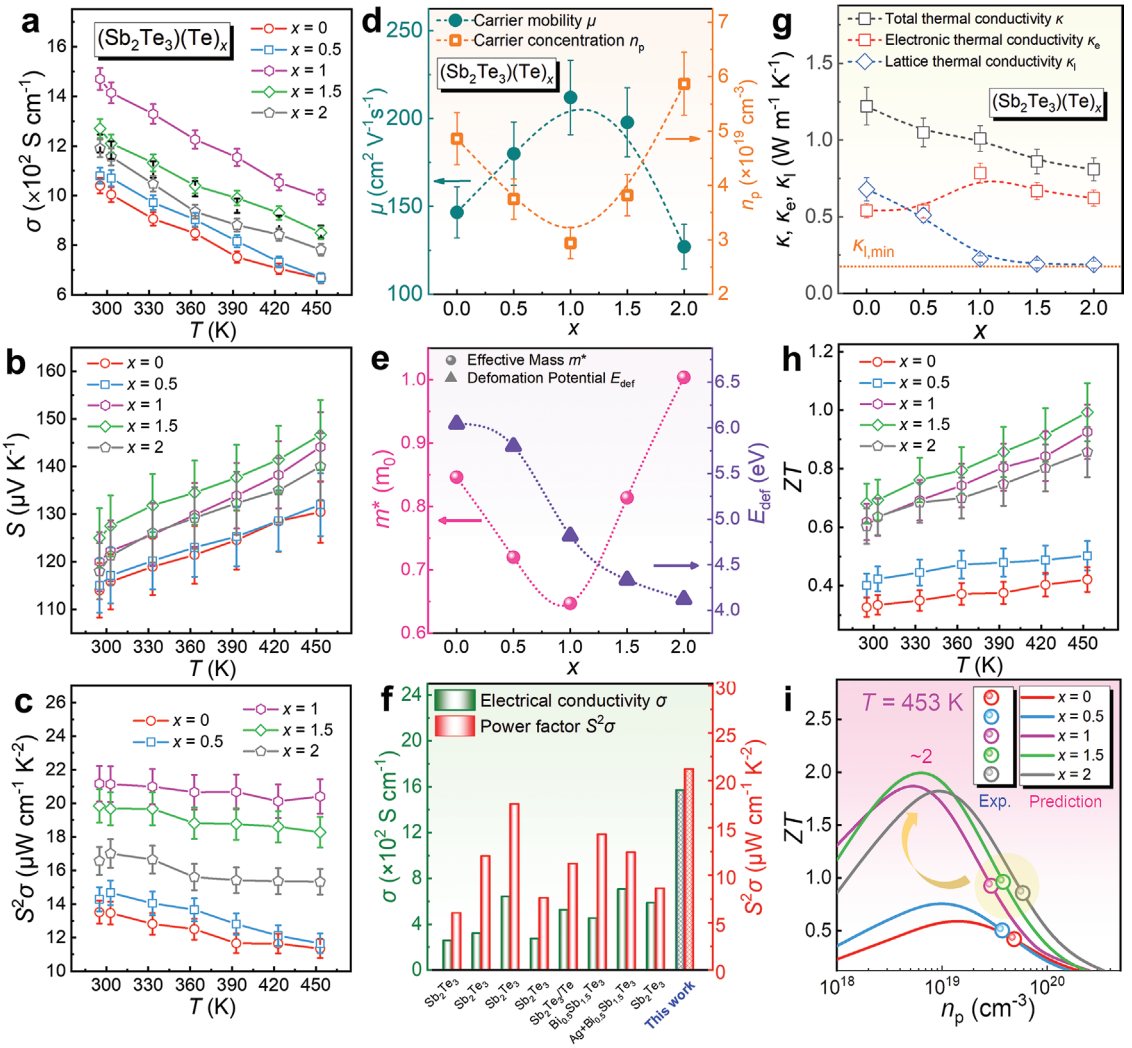

Figure 4. Temperature-dependent a) electrical conductivity σ, b) Seebeck coefficient S, and c) power factor $S^2\sigma$ of $(Sb_2Te_3)(Te)_x$ thin films ($x = 0$, 0.5, 1, 1.5, and 2). d) Carrier density n_p and mobility μ as a function of x. e) Effective mass m^* and deformation potential E_{def} as a function of x. f) Comparison of σ and $S^2\sigma$ between this work and reported literature.[40–42,52,58–61] g) Thermal conductivity κ, electronic thermal conductivity κ_e, and lattice thermal conductivity κ_l as a function of x. h) T-dependent ZT. i) n_p-dependent ZT calculated by a single parabolic band (SPB) model.

to the experimental part in Supporting Information),[32,57] the velocity of the hybrids is decreased with increasing the Te content, which is one of the reasons that cause the decrease of E_{def}. Besides, introducing Te can also affect the grain orientation of Sb_2Te_3 as confirmed by the XRD and SEM results, which is another potential reason that influences the change of E_{def}. These results indicate that there are in fact complex mechanisms for the electrical transport of Sb_2Te_3/Te hybrid thin films, which have not been reported before. Nevertheless, benefiting from the rationally introduced Te, the as-achieved high $S^2\sigma$ is very competitive among the reported literature,[40–42,52,58–61] as shown in Figure 4f.

Figure 4g plots temperature-dependent κ, κ_e, and κ_l as a function of x. The κ was measured by the transient electrothermal technique, as illustrated in Figure S5 (Supporting Information). The κ_e was determined by $\kappa_e = LT\sigma$, where L is the Lorentz number calculated by the SPB model as shown in Figure S6 (Supporting Information), and the κ_l was determined by $\kappa_l = \kappa - \kappa_e$. With increasing the Te content, both κ and κ_l are decreased. Especially, the κ_l for $x \geq 1$ has reached the theoretical minimum κ_l ($\kappa_{l,min}$, ≈0.2 W m^{-1} K^{-1}) calculated by a Debye–Callaway model,[62] which is derived from the strengthened phonon scattering at the dense grain and phase boundaries of Sb_2Te_3 and Te (mainly from the nanosized Te inclusions and a few from the Te crystalline islands) observed by our comprehensive characterizations, as well as the potential point defects such as Sb/Te vacancies and Sb'_{Te}. Figure 4h shows temperature-dependent ZT. As can be seen, a high ZT of ≈1 is observed in $(Sb_2Te_3)(Te)_{1.5}$ at 453 K, ranking the top value among the reported flexible Sb_2Te_3-based thermoelectric films as shown in Table S3 (Supporting Information). The room-temperature ZT of $(Sb_2Te_3)(Te)_{1.5}$ can also reach ≈0.7. Figure 4i shows n_p-dependent ZT calculated by a single parabolic band (SPB) model. Although we have successfully suppressed the n_p to 2.94 × 10^{19} cm^{-3} for $(Sb_2Te_3)(Te)_{1.5}$ thin films, there is still considerable room to further suppress the n_p to ≈1 × 10^{19} cm^{-3} for achieving high peak ZTs of ≈2. Besides, our achieved

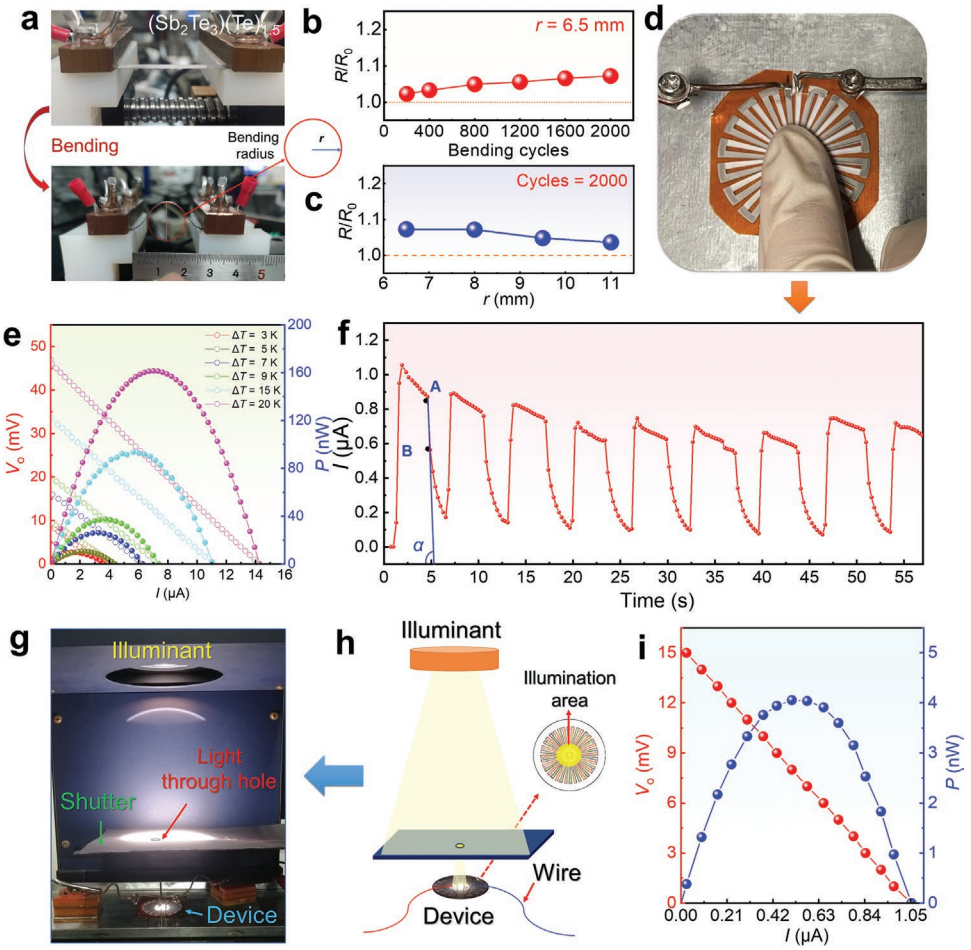

Figure 5. a) Photos of $(Sb_2Te_3)(Te)_{1.5}$ thin film before and during bending. b) R/R_0 of $(Sb_2Te_3)(Te)_{1.5}$ thin film as a function of bending cycle. The r is 6.5 mm. c) R/R_0 of $(Sb_2Te_3)(Te)_{1.5}$ thin film as a function of r after 2000 bending cycles. d) Photo of a fabricated flexible device in the shape of π cyclic. The p-legs are $(Sb_2Te_3)(Te)_{1.5}$ thin films and the n-legs are Bi_2Te_3 thin films. e) Open circuit voltage V_o and output power P of the fabricated device as a function of ΔT. f) Current I as a function of times when a finger taps the center of the device. g) Photo and h) illustration of setting an illumination test. The focused beam hits the center of the device and produces a temperature gradient. i) The as-achieved V_o and P.

thermoelectric properties possess good repeatability, as evidenced by the measured results shown in Figure S7 (Supporting Information).

In addition to the excellent thermoelectric performance, our fabricated $(Sb_2Te_3)(Te)_{1.5}$ hybrid thin films also possess extraordinary flexibility. **Figure 5**a shows the photos of $(Sb_2Te_3)(Te)_{1.5}$ thin film deposited on a polyimide (PI) substrate before and during bending using a homemade automatic film bending instrument and a Keithley 2400 (Movie S1, Supporting Information), and Figure 5b shows the R/R_0 of $(Sb_2Te_3)(Te)_{1.5}$ thin film as a function of bending cycle. The r is maintained as 6.5 mm. Figure 5c shows the R/R_0 of $(Sb_2Te_3)(Te)_{1.5}$ thin film as a function of r after 2000 bending cycles. As can be seen, an ultralow R/R_0 of ≈1.07 can be achieved after 2000 bending cycles with a minimum r of 6.5 mm, indicating extraordinary flexibility. As a reference, the R/R_0 of $(Sb_2Te_3)(Te)_{1.5}$ thin film as a function of r after different bending cycles is plotted in Figure S8 (Supporting Information), and the R/R_0 as a function of bending cycle for different r is shown in Figure S9 (Supporting Information). Compared to previously reported flexible inorganic materials,[63–65] the prepared thin film has excellent flexibility. The reasons can be concluded to be its high crystallinity and dense structure from the microstructure analysis results. Additionally, the nanosized Te inclusions provide more boundaries in the structure, which may help strengthen the mechanical properties and prevent the crack from bending,[66] while the microsized Te crystalline islands may have little effect on the flexibility of the entire thin film. Moreover, we further fabricated a flexible thermoelectric device based on our fabricated $(Sb_2Te_3)(Te)_{1.5}$ hybrid thin films. Figure 5d shows the photo of a fabricated flexible device in the shape of π cyclic. The flexibility of the device is also outstanding confirmed by its measured low R/R_0 of ≈1.003 achieved after 500 bending cycles with a minimum r of ≈7 mm (Figure S10, Supporting Information). The ultralow R/R_0 of the device is even lower than that of the as-fabricated thin film, which is mainly due to its structure with a special center ray arrangement, which can avoid large deformation of the thin films during bending. In addition to the flexible substrate, the high flexibility of the as-fabricated thin films also contributes to the high flexibility of the device. The p-type legs are $(Sb_2Te_3)(Te)_{1.5}$ thin films, and the n-type legs are Bi_2Te_3 thin films. The high-quality n-type Bi_2Te_3 thin film with an average

thickness of ~550 nm was fabricated with high $S^2\sigma$ of 14.14 μW cm^{-1} K^{-2} as shown in Table S4 (Supporting Information), and its characterizations including SEM, EDS, and XRD can be referred to Figure S11 (Supporting Information). The fabrication methods can be referred to the experimental part in Supporting Information. Figure 5e shows the open-circuit voltage V_o and output power P of the fabricated device as a function of ΔT from 3 K to 20 K. The maximum V_o reaches 46.73 mV under a ΔT of 20 K, as well as the highest P of 161.44 nW. As a result, a competitively high ω_{out} of ≈300 μW cm^{-2} can be achieved at a ΔT of 20 K.[44–49] Considering that the ΔT of the human body and the ambient is usually <20 K, such an output power is promising for practical wearable applications. The as-designed flexible device is also appropriate for acting as a sensor. Figure 5f shows the measured current I as a function of times when a finger taps the center of the device. The current was generated through the device as its heat side was touched by a finger, and the other side was left at the ambient temperature in an air-conditioned room (22 °C). The finger left and touched the device at an interval of 3 s. The transient current was 1.07 μA under a ΔT of ≈4 K as the finger touched the hot side, and the current sharply decreased after finger removal. The periodic change of finger touch/leave results in a periodic change of current, stabilized after about 4–5 cycles. Point A shown in Figure 5f is the instant when the finger left the device, and the angle α formed by the tangent line of the arc between Point A and B (Point B is the time point that the finger left after a short moment), and the x-axis is infinitely close to 90 degrees, demonstrating a very rapid reactivity of the device. Figure 5f–h show the photo and the illustration of setting an illumination test based on our fabricated device. The focused beam hits the center of the device and produces a temperature gradient. The illumination results in a change of V_o after a certain illumination time (≈4 min), as shown in Figure 5i. A maximum ΔT of ≈5 K under a solar intensity of 85 mW cm^{-2} was obtained with an illumination time of 4 min. Its V_o and P are ≈16 mV and ≈4.32 nW, demonstrating the possibility of direct conversion of solar energy into electricity. This provides new ideas for the joint development of solar cells and thermoelectric devices.

3. Conclusion

In conclusion, we design Sb_2Te_3/Te hybrid thin films with high thermoelectric performance and extraordinary flexibility, fabricated through a simple and innovative directional thermal diffusion reaction method. The directional thermal diffusion enables excessive Te in Sb_2Te_3, which rationally tunes the n_p and leads to significantly enhanced $S^2\sigma$ of >20 μW cm^{-1} K^{-2}, while the dense grain and phase boundaries between Te and Sb_2Te_3 contribute to a low κ of ≈0.86 W m^{-1} K^{-1}, both leading to a high ZT of ≈1 in $(Sb_2Te_3)(Te)_{1.5}$ at 453 K, which is significantly competitive among the reported flexible thermoelectric films. Besides, an ultralow R/R_0 of ≈1.07 is achieved after 2000 bending cycles with a minimum r of only 6.5 nm, indicating extraordinary flexibility. A rationally designed flexible thermoelectric device composed of $(Sb_2Te_3)(Te)_{1.5}$ thin films as p-type legs and Bi_2Te_3 thin films as n-type legs shows a high ω_{out} of ≈300 μW cm^{-2} by a ΔT of only 20 K, showing high application potential for powering wearable electronic devices and acting as thermal sensors.

4. Experimental Section

The experimental details of this work are provided in the Supporting Information.

Supporting Information

Supporting Information is available from the Wiley Online Library or from the author.

Acknowledgements

M.W., X.-L.S., and Z.-H.Z. contributed equally to this work. This work was supported by the National Natural Science Foundation of China (Grant No. 11604212), the National Natural Science Foundation of Guangdong Province of China (2022A1515010929), Science and Technology plan project of Shenzhen (20200811230408001). ZGC thanks the financial support from the Australian Research Council, HBIS-UQ Innovation Centre for Sustainable Steel project, and QUT Capacity Building Professor Program. The authors are thankful for the assistance on STEM-HAADF observation received from the Electron Microscope Center of the Shenzhen University.

Open access publishing facilitated by Queensland University of Technology, as part of the Wiley - Queensland University of Technology agreement via the Council of Australian University Librarians.

Conflict of Interest

The authors declare no conflict of interest.

Data Availability Statement

The data that support the findings of this study are available from the corresponding author upon reasonable request.

Keywords

devices, flexible, Sb_2Te_3, thermoelectrics, thin films

Received: July 11, 2022
Revised: July 25, 2022
Published online: August 31, 2022

[1] X.-L. Shi, J. Zou, Z.-G. Chen, *Chem. Rev.* **2020**, *120*, 7399.
[2] Y. Xiao, L.-D. Zhao, *Science* **2020**, *367*, 1196.
[3] L. Zhang, X.-L. Shi, Y.-L. Yang, Z.-G. Chen, *Mater. Today* **2021**, *46*, 62.
[4] Q. Xu, B. Deng, L. Zhang, S. Lin, Z. Han, Q. Zhou, J. Li, Y. Zhu, F. Jiang, Q. Li, P. Zhang, X. Zhang, G. Chen, W. Liu, *Cell Rep. Phys. Sci.* **2022**, *3*, 100780.
[5] W.-Y. Chen, X.-L. Shi, J. Zou, Z.-G. Chen, *Small Methods* **2022**, *6*, 2101235.
[6] B. Iezzi, K. Ankireddy, J. Twiddy, M. D. Losego, J. S. Jur, *Appl. Energ.* **2017**, *208*, 758.

[7] T. Cao, X.-L. Shi, J. Zou, Z.-G. Chen, *Microstructures* **2021**, *1*, 2021007.
[8] X. Shi, L. Chen, *Nat. Mater.* **2016**, *15*, 691.
[9] M. Tan, W. D. Liu, X. L. Shi, H. Gao, H. Li, C. Li, X. B. Liu, Y. Deng, Z. G. Chen, *Small Methods* **2019**, *3*, 1900582.
[10] L. M. Goncalves, P. Alpuim, A. G. Rolo, J. H. Correia, *Thin Solid Films* **2011**, *519*, 4152.
[11] B. Poudel, Q. Hao, Y. Ma, Y. Lan, A. Minnich, B. Yu, X. Yan, D. Wang, A. Muto, D. Vashaee, *Science* **2008**, *320*, 634.
[12] Z. Soleimani, S. Zoras, B. Ceranic, S. Shahzad, Y. Cui, *Sustain. Energy Technol. Assessments* **2020**, *37*, 100604.
[13] M. Tan, X.-L. Shi, W.-D. Liu, M. Li, Y. Wang, H. Li, Y. Deng, Z.-G. Chen, *Adv. Energy Mater.* **2021**, *11*, 2102578.
[14] M. Tan, W.-D. Liu, X.-L. Shi, J. Shang, H. Li, X. Liu, L. Kou, M. Dargusch, Y. Deng, Z.-G. Chen, *Nano Energy* **2020**, *78*, 105379.
[15] N. H. Trung, K. Sakamoto, N. V. Toan, T. Ono, *Materials* **2017**, *10*, 154.
[16] X. Zhang, Z. Zeng, C. Shen, Z. Zhang, Z. Wang, C. Lin, Z. Hu, *J. Appl. Phys.* **2014**, *115*, 024307.
[17] I. Hilmi, A. Lotnyk, J. W. Gerlach, P. Schumacher, B. Rauschenbach, *APL Mater.* **2017**, *5*, 050701.
[18] D. W. Newbrook, S. P. Richards, V. K. Greenacre, A. L. Hector, W. Levason, G. Reid, C. H. K. de Groot, R. Huang, *ACS Appl. Energy Mater.* **2020**, *3*, 5840.
[19] D.-H. Kim, G.-H. Lee, O.-J. Kim, *Semicond. Sci. Tech.* **2006**, *22*, 132.
[20] C. Schumacher, K. G. Reinsberg, L. Akinsinde, S. Zastrow, S. Heiderich, W. Toellner, G. Rampelberg, C. Detavernier, J. A. C. Broekaert, K. Nielsch, J. Bachmann, *Adv. Energy Mater.* **2012**, *2*, 345.
[21] J. Yang, H. L. Yip, A. K. Y. Jen, *Adv. Energy Mater.* **2013**, *3*, 549.
[22] J. Kim, M. Zhang, W. Bosze, S.-D. Park, J.-H. Lim, N. V. Myung, *Nano Energy* **2015**, *13*, 727.
[23] S. I. Kim, S. Hwang, J. W. Roh, K. Ahn, D.-H. Yeon, K. H. Lee, S. W. Kim, *J. Mater. Res.* **2012**, *27*, 2449.
[24] R. Venkatasubramanian, *Phys. Rev. B* **2000**, *61*, 3091.
[25] Y. Wang, M. Hong, W.-D. Liu, X.-L. Shi, S.-D. Xu, Q. Sun, H. Gao, S. Lu, J. Zou, Z.-G. Chen, *Chem. Eng. J.* **2020**, *397*, 125360.
[26] F. Rieger, V. Roddatis, K. Kaiser, G. Bendt, S. Schulz, C. Jooss, *Phys. Rev. Mater.* **2020**, *4*, 025402.
[27] S. Xu, X.-L. Shi, M. Dargusch, C. Di, J. Zou, Z.-G. Chen, *Prog. Mater. Sci.* **2021**, *121*, 100840.
[28] X.-L. Shi, W.-Y. Chen, T. Zhang, J. Zou, Z.-G. Chen, *Energy Environ. Sci.* **2021**, *14*, 729.
[29] W.-Y. Chen, X.-L. Shi, J. Zou, Z.-G. Chen, *Nano Energy* **2020**, *81*, 105684.
[30] B. Hu, X.-L. Shi, J. Zou, Z.-G. Chen, *Chem. Eng. J.* **2022**, *437*, 135268.
[31] D.-W. Ao, W.-D. Liu, Y.-X. Chen, M. Wei, B. Jabar, F. Li, X.-L. Shi, Z.-H. Zheng, G.-X. Liang, X.-H. Zhang, P. Fan, Z.-G. Chen, *Adv. Sci.* **2022**, *9*, 2103547.
[32] X. Qian, Y. Xiao, L. Zheng, B. Qin, Y. Zhou, Y. Pei, B. Yuan, S. Gong, L.-D. Zhao, *RSC Adv.*. **2017**, *7*, 17682.
[33] J. Horák, K. Čermák, L. Koudelka, *J. Phys. Chem. Solids* **1986**, *47*, 805.
[34] H. Shang, C. Dun, Y. Deng, T. Li, Z. Gao, L. Xiao, H. Gu, D. J. Singh, Z. Ren, F. Ding, *J. Mater. Chem. A* **2020**, *8*, 4552.
[35] S. J. Kim, J. H. We, B. J. Cho, *Energy Environ. Sci.* **2014**, *7*, 1959.
[36] J. H. We, S. J. Kim, B. J. Cho, *Energy* **2014**, *73*, 506.
[37] W. Zhao, S. Fan, N. Xiao, D. Liu, Y. Y. Tay, C. Yu, D. Sim, H. H. Hng, Q. Zhang, F. Boey, *Energy Environ. Sci.* **2012**, *5*, 5364.
[38] C. Yang, D. Souchay, M. Kneiß, M. Bogner, H. M. Wei, M. Lorenz, O. Oeckler, G. Benstetter, Y. Q. Fu, M. Grundmann, *Nat. Commun.* **2017**, *8*, 16076.
[39] D. Yin, C. Dun, X. Gao, Y. Liu, X. Zhang, D. L. Carroll, M. T. Swihart, *Small* **2018**, *14*, 1801949.
[40] D. Kong, W. Zhu, Z. Guo, Y. Deng, *Energy* **2019**, *175*, 292.
[41] P.-S. Chang, C.-N. Liao, *J. Alloys Compd.* **2020**, *836*, 155471.
[42] H. Shang, T. Li, D. Luo, L. Yu, Q. Zou, D. Huang, L. Xiao, H. Gu, Z. Ren, F. Ding, *ACS Appl. Mater. Interfaces* **2020**, *12*, 7358.
[43] P. LI, X.-L. NIE, Y. TIAN, W.-B. FANG, P. WEI, W.-T. ZHU, Z.-G. SUN, Q.-J. ZHANG, W.-Y. J. ZHAO, *J. Inorg. Mater.* **2019**, *34*, 679.
[44] Y. Lu, Y. Qiu, K. Cai, Y. Ding, M. Wang, C. Jiang, Q. Yao, C. Huang, L. Chen, J. He, *Energy Environ. Sci.* **2020**, *13*, 1240.
[45] L. Wang, Z. Zhang, L. Geng, T. Yuan, Y. Liu, J. Guo, L. Fang, J. Qiu, S. Wang, *Energy Environ. Sci.* **2018**, *11*, 1307.
[46] Y. Lu, Y. Ding, Y. Qiu, K. Cai, Q. Yao, H. Song, L. Tong, J. He, L. Chen, *ACS Appl. Mater. Interfaces* **2019**, *11*, 12819.
[47] R. Tian, C. Wan, Y. Wang, Q. Wei, T. Ishida, A. Yamamoto, A. Tsuruta, W. Shin, S. Li, K. Koumoto, *J. Mater. Chem. A* **2017**, *5*, 564.
[48] L. Wang, Q. Yao, W. Shi, S. Qu, L. Chen, *Mater. Chem. Front.* **2017**, *1*, 741.
[49] Y. Lu, Y. Qiu, Q. Jiang, K. Cai, Y. Du, H. Song, M. Gao, C. Huang, J. He, D. Hu, *ACS Appl. Mater. Interfaces* **2018**, *10*, 42310.
[50] WangWang, B. P. , J. Yang, D. Z. Wang, Z. F. Ren, *J. Am. Chem. Soc.* **2005**, *127*, 13792.
[51] X.-L. Shi, W.-D. Liu, M. Li, Q. Sun, S.-D. Xu, D. Du, J. Zou, Z.-G. Chen, *Adv. Energy Mater.* **2022**, *12*, 2200670.
[52] Z. Wu, X. Chen, E. Mu, Y. Liu, Z. Che, C. Dun, F. Sun, X. Wang, Y. Zhang, Z. Hu, *Adv. Electron. Mater.* **2020**, *6*, 1900735.
[53] Y. M. Zuev, J. S. Lee, C. Galloy, H. Park, P. Kim, *Nano Lett.* **2010**, *10*, 3037.
[54] M. Jin, X.-L. Shi, T. Feng, W. Liu, H. Feng, S. T. Pantelides, J. Jiang, Y. Chen, Y. Du, J. Zou, Z.-G. Chen, *ACS Appl. Mater. Interfaces* **2019**, *11*, 8051.
[55] J. Zhu, X. Zhang, M. Guo, J. Li, J. Hu, S. Cai, W. Cai, Y. Zhang, J. Sui, *npj Comput. Mater.* **2021**, *7*, 116.
[56] J.-S. Liang, X.-L. Shi, Y. Peng, W.-D. Liu, H.-Q. Yang, C.-Y. Liu, J.-L. Chen, Q. Zhou, L. Miao, Z.-G. Chen, *Adv. Energy Mater.* **2022**, *12*, 2201086.
[57] H. Zhang, Y. Cheng, M. Tang, X. Chen, G. Ji, *Comp. Mater. Sci.* **2015**, *96*, 342.
[58] S. Shen, W. Zhu, Y. Deng, H. Zhao, Y. Peng, C. Wang, *Appl. Surf. Sci.* **2017**, *414*, 197.
[59] E. M. F. Vieira, J. Figueira, A. L. Pires, J. Grilo, M. F. Silva, A. M. Pereira, L. M. Goncalves, *J. Alloys Compd.* **2019**, *774*, 1102.
[60] E. M. F. Vieira, A. L. Pires, J. P. B. Silva, V. H. Magalhães, J. Grilo, F. P. Brito, M. F. Silva, A. M. Pereira, L. M. Goncalves, *ACS Appl. Mater. Interfaces* **2019**, *11*, 38946.
[61] A. Kobayashi, R. Konagaya, S. Tanaka, M. Takashiri, *S.Actuat. A-phys.* **2020**, *313*, 112199.
[62] C. Chiritescu, C. Mortensen, D. G. Cahill, D. Johnson, P. Zschack, *J. Appl. Phys.* **2009**, *106*, 073503.
[63] Z. Gao, Q. Yang, P. Qiu, T.-R. Wei, S. Yang, J. Xiao, L. Chen, X. Shi, *Adv. Energy Mater.* **2021**, *11*, 2100883.
[64] S. He, Y. Li, L. Liu, Y. Jiang, J. Feng, W. Zhu, J. Zhang, Z. Dong, Y. Deng, J. Luo, W. Zhang, G. Chen, *Sci. Adv.* **2020**, *6*, eaaz8423.
[65] B. Wu, Y. Guo, C. Hou, Q. Zhang, Y. Li, H. Wang, *Adv. Funct. Mater.* **2019**, *29*, 1900304.
[66] Z. Li, L. Fu, J. Peng, H. Zheng, X. Ji, Y. Sun, S. Ma, A. Shan, *Mater. Charact.* **2020**, *159*, 109989.